Journal of Alloys and Compounds 790 (2019) 1127–1136

Contents lists available at ScienceDirect

Journal of Alloys and Compounds

journal homepage: http://www.elsevier.com/locate/jalcom

Highly transparent, conducting, body-attachable metallized fibers as a flexible and stretchable film

Yong Il Kim [a, 1], Seongpil An [b, 1], Min-Woo Kim [a], Hong-Seok Jo [a], Tae-Gun Kim [a], Mark T. Swihart [c], Alexander L. Yarin [b, **], Sam S. Yoon [a, *]

[a] School of Mechanical Engineering, Korea University, Seoul, 24801, Republic of Korea
[b] Department of Mechanical and Industrial Engineering, University of Illinois at Chicago, 842 West Taylor Street, Chicago, IL 60607-7022, United States
[c] Department of Chemical & Biological Engineering and RENEW Institute, University at Buffalo, The State University of New York, Buffalo, NY 14260-4200, United States

ARTICLE INFO

Article history:
Received 21 November 2018
Received in revised form
8 March 2019
Accepted 9 March 2019
Available online 13 March 2019

Keywords:
Silver-plated fibers
Core-shell fibers
Flexible electronics
Transparent conducting films and heaters

ABSTRACT

Core–shell-structured silver-electroplated nickel microfibers were fabricated via electrospinning and subsequent electroplating for applications including transparent conductive films (TCFs) and heaters. Fabrication protocol generated self-fused junctions at the intersections of overlapping micro-nanofibers. This reduced contact resistance between wires, yielding remarkably high electrical conductivity, which is highly desirable for the aforementioned applications. A very low sheet resistance of less than 0.2 Ω sq^{-1} with a high transmittance of over 92% was achieved in these structures. A cactus-like morphology of silver-plated microfibers, which dramatically increases surface-to-volume (*S*/*V*) ratio and should produce electric field concentration at silver nanowire tips, was also demonstrated. This unique surface morphology could be promising for energy and environmental applications that require large interfacial areas and electric field concentration, but yielded lower transmittance than smooth wires. These cactus-like microfibers were further coated with Cu and Pt to produce hierarchically-structured multimetallic microfibers. The low-resistivity transparent silver micro-nanofiber films exhibited good heating and mechanical properties, as demonstrated in bending and stretching tests. A record high temperature of 209 °C was achieved with a transparent heater based on the Ag microfibers.

1. Introduction

One-dimensional (1D) Ag microstructures, such as Ag nanowires (AgNWs), are of great interest because of their potential use in various electronic devices [1-8]. Nanoscale 1D structures of Ag, which has the highest electrical and thermal conductivities among all elemental metals, are among the most valuable materials for transparent conductive electrodes (TCEs) [9,10]. Micro- and nanoscale electrode performance and reliability depend on the percolative structures of TCE materials [11,12]. An ideal percolative cluster with a continuous conducting network structure can confer high electrical conductivity to electrodes with minimal losses in transparency [9,13].

Several methods have been employed to fabricate 1D Ag microstructures, including hydrothermal [14,15], microwave-assisted [16,17], electrochemical [18], UV- [19,20], and polyol-based approaches [21,22]. The polyol method is currently recognized as the most promising approach in terms of cost and scalability. This process is based on the growth of Ag nanoparticles (NPs) via a reaction between metallic salts and a polyol. However, the approach is insufficiently mature for large-scale commercial implementation.

We recently explored the fabrication of percolative TCEs via electrospinning and electroplating [11,12]. Electrospinning produces polymer nanofibers (NFs) that can be applied in various fields, including biomedical- and energy-related industries [23-28]. Electrospun NFs can be electroplated to form metallized NFs after their surfaces are seeded with metal NPs by either dip-coating or sputtering. Subsequent oxidation of the metal fibers converts them into metal oxides that can be used in various energy and environmental applications requiring semi-conducting properties and high interfacial areas [11,12,28-34]. A percolation model that describes the electrical and optical behaviors of 1D nanomaterials was recently reported based on the renormalization group theory

* Corresponding author.
** Corresponding author.
E-mail addresses: ayarin@uic.edu (A.L. Yarin), skyoon@korea.ac.kr (S.S. Yoon).
[1] Yong Il Kim and Seongpil An contributed equally.

https://doi.org/10.1016/j.jallcom.2019.03.154
0925-8388/

technique of the classical percolation theory [11,35,36].

Transparent conducting networks of NFs (about 100 nm in diameter) can also be formed via the electrospinning and solution blowing of polymer blends containing conducting polymers [37]. Such a NF network reached a moderate sheet resistance (R_s) value of 8.4 kΩ sq^{-1} with 84% optical transmittance.

Sinha-Ray et al. [29] presented initial studies on the production of Ag-plated NFs by electrospinning and electroplating. These fibers were used as heat-removing mats for microelectronic cooling applications. However, the electrical properties of these NFs were not reported, and transparent conductive films (TCFs) and heating applications were not discussed. We demonstrate herein the enhanced electrical properties of electrospun and Ag-plated NFs, surpassing those of other 1D nanomaterials in terms of transparency and electrical conductivity [11]. In addition, a cactus-like nanotextured surface on Ag microfibers (MFs) was achieved by manipulating the electroplating precursor formulation. Because of the dramatically increased surface area of the fibers, the nanotextured AgMFs show great promise for applications requiring large interfacial area of Ag or electric field concentration at sharp Ag tips.

2. Experimental

2.1. Materials

2.1.1. Electrospinning

Polyacrylonitrile (PAN, $M_w = 150$ kDa) and *N*,*N*-dimethylformamide (DMF, 99.8%) were purchased from Sigma-Aldrich (USA). Ni foil (99.9%, thickness of 20 μm), used as a material for the Ni frame (as a collector of electrospun fibers) and as the anode electrode (in the Ni-electroplating process), was purchased from Wellcos Corporation (Republic of Korea).

2.1.2. Ni-electroplating

Ni (II) sulfamate tetrahydrate [$Ni(SO_3NH_2)_2 \cdot 4H_2O$, 98%], boric acid ($H_3BO_3$, 99.97%), sodium hydroxide solution (NaOH, 1.0 M), and formaldehyde (CH_2O, 35%) were purchased from Sigma-Aldrich (USA). Single-distilled deionized (DI) water purchased from Samchun Pure Chemical (Republic of Korea) was used for the preparation of the electroplating solutions.

2.1.3. First Ag-electroplating

Ag nitrate ($AgNO_3$, 99%), potassium hydroxide (KOH, 85%), ammonium hydroxide (NH_4OH, 99.9%), and nitric acid (HNO_3, 70%) were purchased from Sigma-Aldrich (USA). Sugar (Beksul, Republic of Korea) was obtained from a local market. Platinum (Pt) plates, used as the anode material (in the Ag/Cu/Pt electroplating process), were obtained from HanTeck PMC (Republic of Korea).

2.1.4. Second Ag-electroplating

The KS-700 solution, potassium argentocyanide [$KAg(CN)_2$], and potassium cyanide (KCN, 98%) were obtained from Poongwon Chemical (Republic of Korea). The KS-700 solution consisted of 6% (v/v) sodium borate ($B_4Na_2O_7$), 79% (v/v) water, 10% (v/v) potassium phosphate (KH_2PO_4), and 5% (v/v) phosphates.

2.1.5. Cu-electroplating

Sulfuric acid (H_2SO_4, 99%) was purchased from Matsunoen Chemicals (Japan). Hydrochloric acid (HCl, 37%) and Cu(II) sulfate ($CuSO_4$, 99%) were purchased from Sigma-Aldrich (USA).

2.1.6. Pt-electroplating

A chloroplatinic acid solution (H_2PtCl_6, 5 wt% in distilled water) was obtained from HanTeck PMC (Republic of Korea).

2.2. Prefabrication of polyacrylonitrile nanofibers

First, an 8 wt% yellow PAN solution was prepared by dissolving PAN powder in DMF. The solution was stirred for 24 h at 25 °C until it became homogenous. As shown in step I of Fig. 1, the PAN solution was then injected with an 18-gauge needle (Nordson EFD, USA) using a syringe pump (Legato 100, KD Scientific Inc., USA) with a fixed flow rate of $Q_{es} = 200$ μL h^{-1}. A direct current (DC) voltage of $V_{es} = 6.5$ kV was applied to the needle using a DC power supply (EP20P2, Glassman High Voltage Inc., USA). Electrospinning of the Taylor cone-like PAN jet at the needle tip produced a continuous single nanofiber (NF), which was deposited on a Ni frame with a square open area of 3 cm × 3 cm and a frame width of 1 cm. The deposition time (or electrospinning time), t_{es}, was set to 5 s to obtain a thin NF mat with high transparency. Note that the frame-type substrate was used to obtain freestanding NFs.

2.3. Fabrication of Ni and Ni/Ag-electroplated fibers

The Ni-electroplating solution was prepared by blending 80 g $Ni(SO_3NH_2)_2 \cdot 4H_2O$, 6 g H_3BO_3, and 200 mL DI water [29]. The pH of the solution was adjusted to 4.5 by adding NaOH and measured using pH paper (Advantec, Japan). The solution was blended using a magnetic stirrer for 24 h at room temperature before use. Note that all electroplating solutions were stored in dark brown glass bottles at room temperature and used less than 20 times.

For the first Ag-electroplating solution, two different solutions were prepared: solution A and solution B [29]. For preparing solution A, 0.5 g $AgNO_3$ and 0.5 g KOH were each dissolved in 5 mL of DI water. Next, these two solutions were mixed, and 1.25 mL of NH_4OH was added. Solution A was stirred for 24 h. For preparing solution B, sugar (2.25 g), 0.1 mL HNO_3, and 25 mL DI water were mixed. Solution B was boiled at 100 °C and stirred with a magnetic stir bar for 24 h. Finally, solution A and solution B were blended and stirred for 10 min. After the plating solution was prepared, the Ag-electroplating experiment proceeded immediately.

The second Ag-electroplating solution was prepared as follows: 250 mL KS-700 solution was mixed with 200 mL DI water and held at 45 °C. Next, 60 g $KAg(CN)_2$ was added to the solution and the total volume was adjusted to 500 mL while the temperature was maintained at 45 °C. Then, this solution was heated to 65 °C and 100 g of KCN was added to it. The pH of the solution was then adjusted to 4.5 by adding NaOH. This solution was also blended and stored in a dark brown glass bottle at room temperature and used less than 20 times for electroplating.

Prior to the electroplating process, the freestanding PAN NFs were lightly sputtered with Pt (MSP-1S, Vacuum Device Inc., Japan) [29,38]. According to our previous work [11], a Pt layer of a few nanometers in thickness layer sputtered on the PAN NFs is sufficient to provide the electrical conductivity required to trigger the electroplating of the polymer NFs. As shown in step II of Fig. 1, the PAN NFs were first electroplated with Ni, followed by Ag. The Ni-electroplated fibers (NiEFs) were prepared as follows: The PAN NFs (suspended on a Ni frame) and a piece of Ni foil (3 cm × 3 cm) were immersed in the electroplating solution as the cathode and anode, respectively. An electric current (current density $I_{ep} = 0.20$ A cm^{-2} based on the total mat area of the PAN NFs) was sustained by a power supply (SPS-1820, GW Instek, Taiwan) for 60 s. The distance between the frame and the foil was 2 cm. The plated sample was rinsed with 40% (v/v) CH_2O (diluted in DI water) and DI water for 10 min and 5 s, respectively. Finally, the rinsed sample was dried under an Ar atmosphere for a few minutes to prevent oxidation. As a result, the electroplating of Ni yielded Ni-wrapped PAN NFs. The NiEFs were then electroplated with Ag.

Most of the experimental conditions for the Ag-electroplating

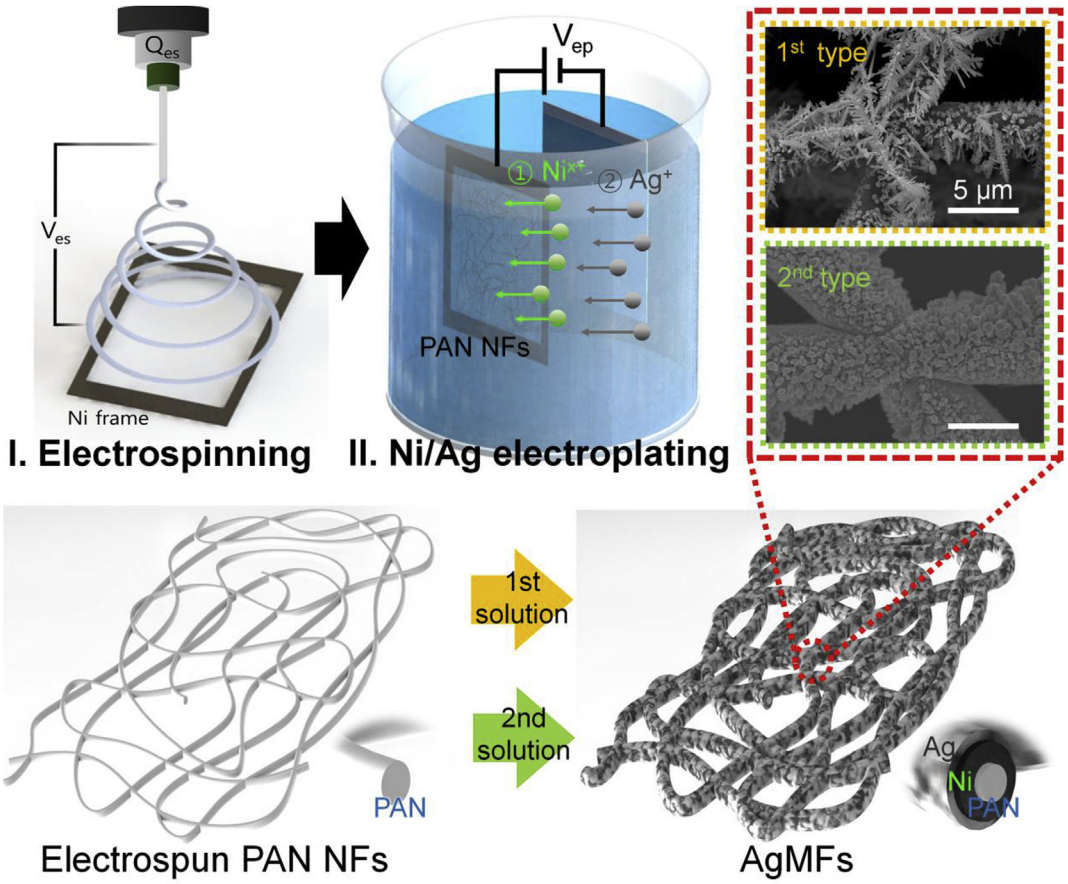

Fig. 1. Schematic of the fabrication process of the AgMFs.

were the same as those used for the Ni-electroplating. The Ag-electroplating solution and the Pt plate for the anode were used instead of the Ni-electroplating solution and Ni foil, respectively. The first Ag-electroplating was conducted with $I_{ep} = 0.125\ A\ cm^{-2}$ and different electroplating times of $t_{ep} = 10$ and 60 s. Electroplating of Ag yielded uniquely shaped Ag-wrapped NiEFs, as shown in Fig. 1. The second Ag-electroplating was conducted on NiEFs with different electroplating voltages of $V_{ep} = 2$, 6, and 8 V, and the electroplating times of $t_{ep} = 1$, 3, 5, and 10 s. In addition, according to the different Ag-electroplating methods, two types of Ag microfibers (MFs) were fabricated as shown in Figs. 1 and 2.

2.4. Fabrication of Ni/Ag/Cu/Pt-electroplated fibers

The Cu-electroplating solution was prepared by mixing 10 g H_2SO_4, 1 g HCl, 32 g $CuSO_4$, and 20 g CH_2O with 200 mL of DI water [29,39]. The solution was blended using a magnetic stirrer for 24 h at room temperature. The Cu-electroplating was performed on the first AgMFs by applying a voltage of 3 V for 30 s. A Pt plate was used as the anode. The Ni/Ag/Cu-electroplated fibers were then rinsed with 40% (v/v) CH_2O (diluted in DI water) and DI water for 10 min and 5 s, respectively. The mat was then dried under an Ar atmosphere for a few minutes to prevent oxidation.

The Pt-electroplating solution was obtained by adding DI water to 160 mL of 5% H_2PtCl_6 until the total solution volume reached 1 L [12]. The solution was magnetically stirred for one day at room temperature to stabilize. The pH was adjusted to 1.5 by adding H_2SO_4 or NaOH. The Pt-electroplating conditions for the Ni/Ag/Cu/Pt were $I_{ep} = 0.2\ A\ cm^{-2}$ and $t_{ep} = 90$ min, using a Pt plate as the anode.

2.5. Characterization

The surface morphologies of the samples were analyzed by scanning electron microscopy (SEM) using a field-emission SEM system with energy-dispersive X-ray spectroscopy (FE-SEM/EDX, Quanta 250 FEG, FEI). The average diameter of the AgMFs was measured using I'MEASURE3 software (IngPlus, Republic of Korea); 100 fibers from the SEM images were measured and the average value was computed. The roughness values R_a of the AgMFs were obtained by an optical profiler (OP, NT-1100, Veeco, USA). The arithmetic average roughness values were obtained using Vision 3.0 software (Veeco, USA); 10 fibers from the optical images were measured and the average value was used. The surface areas of composites were determined from N_2 adsorption and desorption isotherms measured using a volumetric adsorption apparatus (Tristar 3000, Micromeritics). Before N_2 adsorption measurements the sample was pretreated at 70 °C for 48 h under high vacuum ($<10^{-6}$ Torr). X-ray diffraction (XRD, SmartLab, Rigaku) and X-ray photoelectron spectroscopy (XPS, X-tool, ULVAC-PHI) were used to analyze the crystalline structures and surface elemental compositions of the AgMFs. The transparency T_r, which is based on air, was measured for a square area of 2 cm × 0.8 cm in air using ultraviolet–visible spectrophotometry (Optizen POP, Mecasys). The R_s values were obtained by the four-point probe method with a sheet resistance meter (FPP-400, Dasol Eng) based on a dual-configuration procedure. The value of R_s was the average value of 10 randomly measured R_s values at different locations. The AgMF sample for cross-sectional imaging was prepared using a dual-beam focused ion beam (FIB) system (SCIOS, FEI) and the sample was analyzed by transmission electron microscopy (TEM, JEM

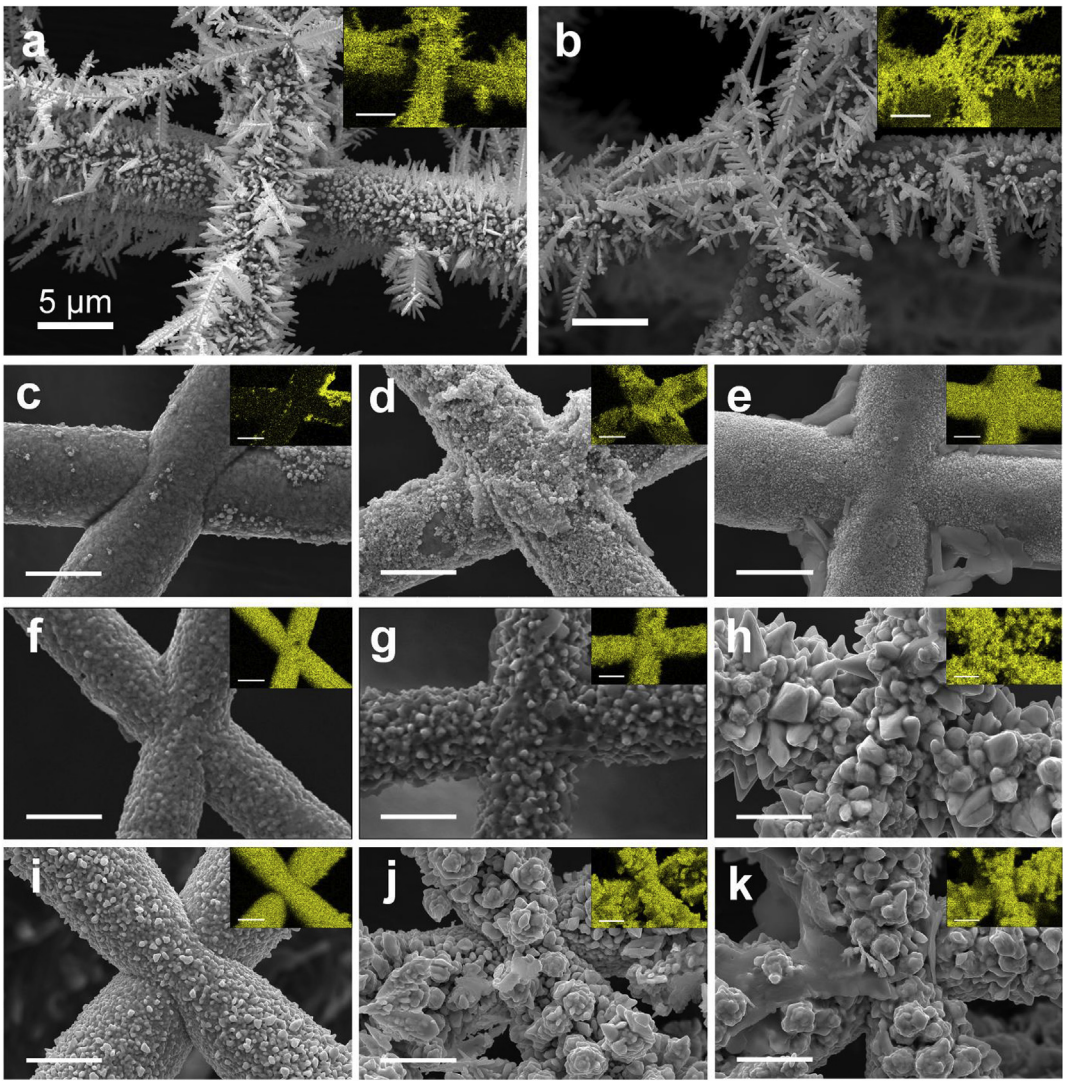

Fig. 2. SEM and (in the insets) silver elemental mapping images of AgMFs for the different Ag-electroplating methods, and different values of t_{ep}, and V_{ep}: (a–b) The first Ag-electroplating method with a fixed $V_{ep} = 8$ V and different (a) $t_{ep} = 10$ s and (b) $t_{ep} = 60$ s. (c–e) The second Ag-electroplating method with a fixed $V_{ep} = 2$ V and different (c) $t_{ep} = 1$ s, (d) $t_{ep} = 3$ s, and (e) $t_{ep} = 10$ s. (f–h) The second Ag-electroplating method with a fixed $V_{ep} = 5$ V and different (f) $t_{ep} = 1$ s, (g) $t_{ep} = 3$ s, and (h) $t_{ep} = 10$ s. (i–k) The second Ag-electroplating method with a fixed $V_{ep} = 8$ V and different (i) $t_{ep} = 1$ s, (j) $t_{ep} = 3$, and (k) $t_{ep} = 10$ s. Yellow dots in the elemental mapping images represent Ag. (For interpretation of the references to color in this figure legend, the reader is referred to the Web version of this article.)

2100F, JEOL Inc.). In the FIB process, rough cuts were performed with a beam current of 7–15 nA at 30 kV, and final cleaning was conducted with a beam current of 3–7 nA at 30 kV to ensure minimal ion damage. For the stretching test (cf. Movie S1), an AgMF mat was first transferred onto an Eco-flex film with 1 mL of Eco-flex for adhesion and was dried for 24 h. One end of the sample was fixed and the other end of the sample was stretched using a syringe pump (LEGATO100, KDScientific, USA) with a fixed speed of cyclic motion. Simultaneously, the resistance changes were recorded by a digital multimeter (3256, Hioki) during stretching. For the bending cycle test, an AgMF mat was transferred onto a polyethylene terephthalate (PET) film; a drop of ethanol was first dripped onto the film and then the AgMF mat was placed onto the PET film using tweezers. In a short time, the ethanol between the fibers and PET film was evaporated, thus facilitating the adhesion of the fibers to the PET film. The AgMF mat adhered to the PET film during the bending test and did not delaminate. The sample was repetitively bent around one axis with a bending radius of 4 mm and frequency of 2 Hz. The resistances between several pairs of points, equally spaced in the direction perpendicular to the axis, were measured. For LED operation, LEDs were purchased from GreenMax (0.24 W at 12 V, Republic of Korea). Six LEDs were connected in series and a voltage of 6 V was applied to the circuit. The heating performance was examined using a power supply (SPS-1820, GW Instek, Taiwan), thermocouple, and data recorder (MV1000, Yokogawa). To minimize the IR loss, 2.3-mm-diameter 10-cm-long Cu wires were used in the heating experiments with the maximum IR loss of only 0.002%. The heating performance under stretching (cf. Movie S2) was observed by an infrared (IR) camera (FLIR-E63900, FLIR, Wilsonvile, USA), where AgMFs on Eco-flex were stretched by a syringe pump at a constant speed of movement. Note that all the mechanical and optical experiments mentioned above were conducted at ambient conditions of room temperature and 20–30% humidity.

Supplementary video related to this article can be found at https://doi.org/10.1016/j.jallcom.2019.03.154.

3. Results and discussion

Scanning electron microscopy (SEM) images of the silver

microfibers (AgMFs) are presented in Fig. 2 (low magnification SEM images are presented in Fig. S1). Dendritic morphologies are produced using the first Ag-electroplating solution, as revealed in Fig. 2a and b. In contrast to the second Ag-electroplating process (cf. Fig. 2c–k), highly textured cactus-like surfaces were observed with the first method. Although the second Ag-electroplating process also produced uniquely textured surfaces, the first induced a distinctly different morphology. Different trends were observed with respect to T_r and R_s for the two fiber types (see Tables 1 and 2). Thus, the choice of the Ag-electroplating method should be dictated by the intended applications of the AgMFs. For example, the first process appears to be more appropriate for catalytic and electrocatalytic applications, while the second process is more appropriate for transparent conductive electrodes (TCEs) where a balance between high T_r and low R_s is necessary. Subsequent mechanical and thermal experiments presented in this study were based on the second AgMFs for application to TCEs.

Using the second Ag-electroplating method with an electroplating voltage of $V_{ep} = 2$ V (Fig. 2c–e), granular island-like clusters were initially formed on the outer surfaces of the Ni-electroplated fibers (NiEFs). In addition, as the electroplating time (t_{ep}) increased from 1 to 10 s, the overall surface of the fibers was gradually covered by Ag (Fig. 2c–e). In contrast, at $V_{ep} = 6$ and 8 V, a short $t_{ep} = 1$ s was sufficient to fully cover the entire outer surface of the NiEFs with Ag (Fig. 2f–k); at $t_{ep} = 1$ s ($V_{ep} = 5$ V), increased surface roughness (R_a) was observed compared with the basic NiEFs ($t_{ep} = 0$ s) (Table S1). As t_{ep} increased to 5 s, the Ag layer became thicker while the R_a value decreased. However, the value of R_a significantly increased again at $t_{ep} = 10$ s. The complete Ag plating of the Ni fibers is attributed to the enhanced metallic bonding of the fibers at the fiber junctions, as well as the higher conductivity of Ag relative to that of Ni, which caused a significant decrease in the electrical contact resistance at the junctions. For example, at $V_{ep} = 5$ V, R_s decreased significantly from 3.01 to 0.49 Ω sq^{-1} when t_{ep} increased from 0 (which corresponds to the bare NiEFs) to 1 s (Table 2). Note that R_s decreased to 0.05 Ω sq^{-1} when t_{ep} increased from 0 to 10 s, while the average thickness (D_{avg}) of the AgMFs increased from 3.47 to 12.6 μm. As V_{ep} increased, the grain size and corresponding growth rate also increased considerably. The formation of a bump-like Ag texture became more pronounced as V_{ep} increased from 6 to 8 V (cf. Fig. 2f–k).

Results of N_2 physisorption measurements for NiEFs and AgMFs, presented in Fig. S2, show type IV characteristic curves. Both macro and micro pores of NiEFs are evident from the hysteresis at very high relative pressure. On the other hand, only micropores are present on AgMFs, based on the hysteresis in the N_2 adsorption-desorption curves at lower relative pressure. The surface areas obtained from these isotherms by Brunauer-Emmett-Teller (BET) analysis, along with pore volume and pore size, are presented in Table S2.

To further characterize Ag deposition on the fiber surface, X-ray diffraction (XRD) analysis was conducted (Fig. S3). The XRD sample characterized here comprised AgMF deposited by the second method with $V_{ep} = 5$ V and $t_{ep} = 3$ s. The XRD pattern exhibited four main peaks at $2\theta = 38.0°$, 44.1°, 64.3°, and 77.3°, corresponding to diffraction from the (111), (200), (220), and (311) planes of Ag, respectively (JCPDS No. 04-0783). In addition, the surface composition of the AgMFs and the chemical states of Ag were characterized by X-ray photoelectron spectroscopy (XPS) analysis. The complete survey spectra for the AgMFs are shown in Fig. S4a, revealing the presence of Ag, C, and O. The C 1*s* peak at 284 eV was used as a reference for calibration of binding energies. The small O peak arose from some oxidation during the manufacturing processes [29,40]. The Ag 3*d* XPS spectrum contains two sharp peaks (Fig. S4b) at 368.1 and 374.3 eV, corresponding to Ag $3d_{5/2}$ and Ag $2d_{3/2}$, respectively. The difference between the energies of the Ag $3d_{5/2}$ and Ag $2d_{3/2}$ peaks was 5.8 eV, corresponding metallic Ag^0 [41].

Fig. 3 shows cross-sectional transmission electron microscopy (TEM) and corresponding EDX elemental mapping images of the second AgMFs and Ni/Ag/Cu/Pt MFs (where the first Ag-electroplating method was used). The samples for TEM analysis were prepared by the focused ion beam (FIB) milling method (cf. Sec. 2.5.). The sequential electroplating of Ni and Ag yielded intact core–shell-structured metallized fibers. The elemental mapping results revealed that the fiber contained a middle Ni shell on the interior PAN core and an outer Ag shell. The thicknesses of the outermost Ag, middle Ni, and innermost PAN layers are 1.53, 1.05, and 0.75 μm (0.37 μm radius of PAN fiber), respectively (Fig. 3a). The thickness of both the Ni and Ag layers can be controlled by changing the electroplating conditions (cf. Sec. 2.3.). The selected-area electron diffraction (SAED) pattern (shown in Fig. S5) also confirmed that the electroplated fibers were covered by Ag with a face-centered cubic structure [42].

Fig. 3e–j show cross-sectional TEM and elemental mapping images of the Ni/Ag/Cu/Pt multilayered MF. Outside the Ni core, the cactus-like Ag layer is formed by the first Ag-electroplating (Fig. 3g). Then, a thick but discontinuous Cu layer was deposited on the Ag layer, and Pt was plated where the Cu layer had not grown. Therefore, the overall shape of the fibers is smoothly rounded despite the hierarchical structure of the Cu layer, as shown in Fig. S6. The thickness of each metal layer can be varied by adjusting plating parameters (cf. Sec. 2.4.).

The Ag shell provides high electrical conductivity to the metallized fibers, which exhibits remarkably low R_s values (Fig. 4 and Table 2). High transparency is also observed (Fig. 4a and c). Note that the $t_{ep} = 0$ s case in Fig. 4 corresponds to nickel electroplating only, without silver-electroplating. These characteristics are illustrated by the electrical conductivity–transmittance plot in Fig. 4b. A common figure of merit (FoM) used to assess and compare the performance of transparent electrodes is defined as FoM = T_r^{10}/R_s (Ω^{-1}) [43]. The FoM of the AgMFs prepared by the second method is up to 1.2 Ω^{-1}. The reported FoM of Cu-electroplated wires [11] reached 1.8 Ω^{-1}; FoM of Cu nanofibers [44] was 0.15 Ω^{-1}; FoM of Ag nanowires [45] was 0.012 Ω^{-1}; FoM of gold nanofibers [46] was 0.0094 Ω^{-1}; FoM of graphene [47] was 0.009 Ω^{-1}; FoM of PEDOT:PSS [48] was 0.0042 Ω^{-1}; FoM of single-walled carbon nanotubes [49] was 0.00084 Ω^{-1}. Clearly, the FoM of the AgMFs is among the highest reported, very similar to the maximum FoM reported for CuEWs, and with a different T_r vs. R_s tradeoff curve from the CuEWs, such that the AgMFs achieve previously unachievable low values of

Table 1
T_r at the wavelength λ = 550 nm and the R_s values for the 1st AgMFs ($I_{ep} = 0.125$ A cm^{-2}).

Case	Experimental result	
t_{ep} (s)	T_r (%)	R_s (Ω sq^{-1})
10	25	0.150 ± 0.019
60	6	0.221 ± 0.034

Table 2
T_r at the wavelength λ = 550 nm and R_s values for the 2nd AgMFs ($V_{ep} = 5$ V).

Case	Experimental result		
t_{ep} (s)	D_{avg} (μm)	T_r (%)	R_s (Ω sq^{-1})
0	3.47 ± 0.17	96	3.01 ± 1.05
1	5.17 ± 0.26	95	0.49 ± 0.01
3	6.50 ± 0.40	92	0.18 ± 0.03
5	8.35 ± 0.54	91	0.11 ± 0.04
10	12.60 ± 2.27	84	0.05 ± 0.01

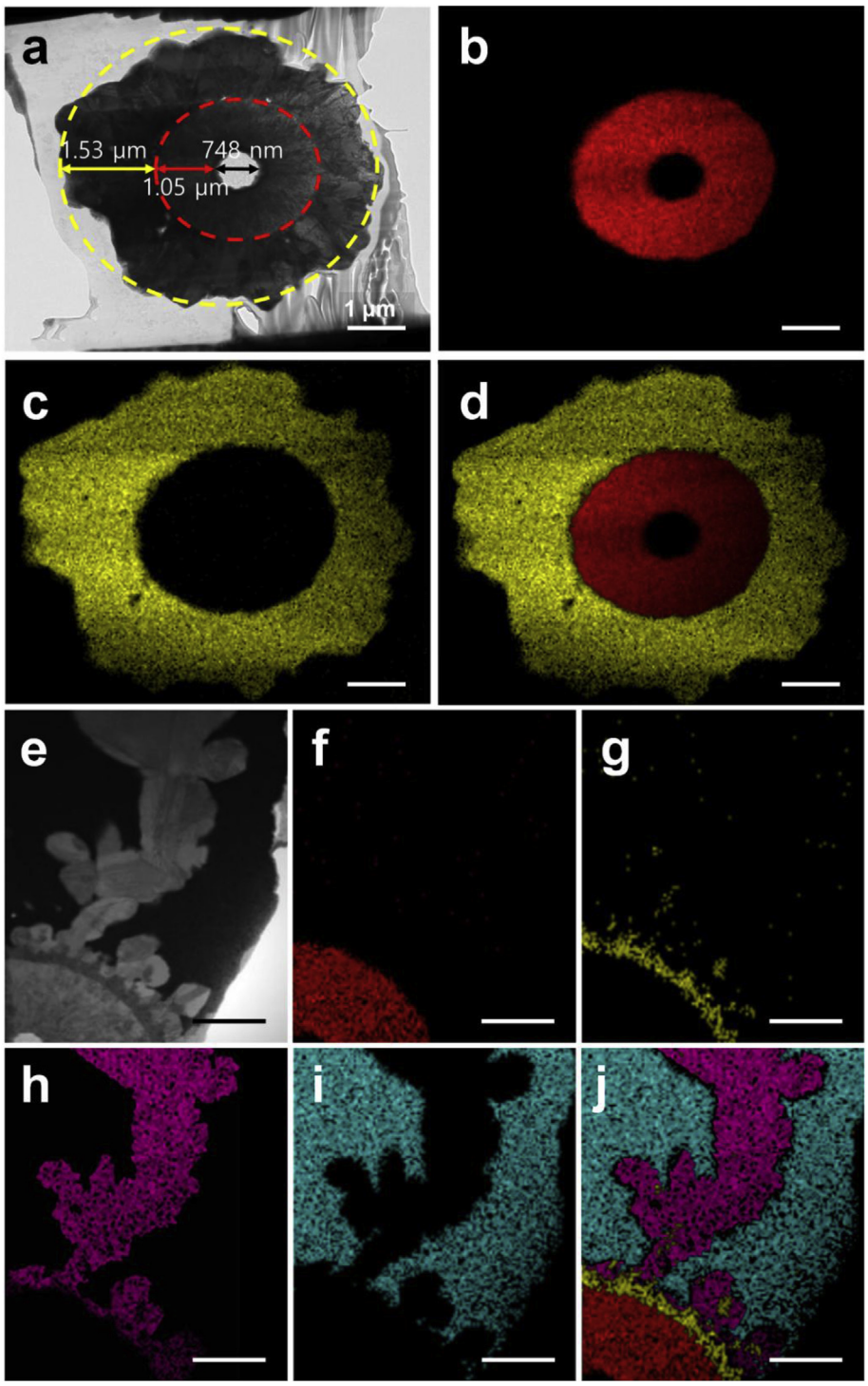

Fig. 3. Cross-sectional TEM images of (a) the second AgMF, and (e) the Ni/Ag/Cu/Pt multilayered MF. Elemental mapping images of (b–d) the second AgMF, and (f–j) the Ni/Ag/Cu/Pt multilayered MF. Red, yellow, pink, and cyan dots in the elemental mapping images represent Ni, Ag, Cu, and Pt, respectively. (For interpretation of the references to color in this figure legend, the reader is referred to the Web version of this article.)

R_s for high T_r.

Moreover, our AgMFs possess high T_r and low R_s compared to conventional AgNW samples, cf. Table S3, which compares the substrates used in each method of producing transparent conducting films. These substrates have transparency values in the 80–91% range, while the AgMF film is free-standing and does not require a substrate, as demonstrated in Fig. 5 [50-52]. This free-standing feature is important, because it facilitates flexibility while minimizing the mass of the electrode. The T_r values of the AgMFs in the 400–800 nm wavelength (λ) range are almost constant, which is advantageous for their use in various optoelectronic applications, including solar energy harvesting, lighting, and display applications [53].

Table 3 compares the T_r and R_s values measured here with those from previous studies by An et al. [11,12,38]. The differences in the electrospinning and electroplating conditions, such as t_{es}

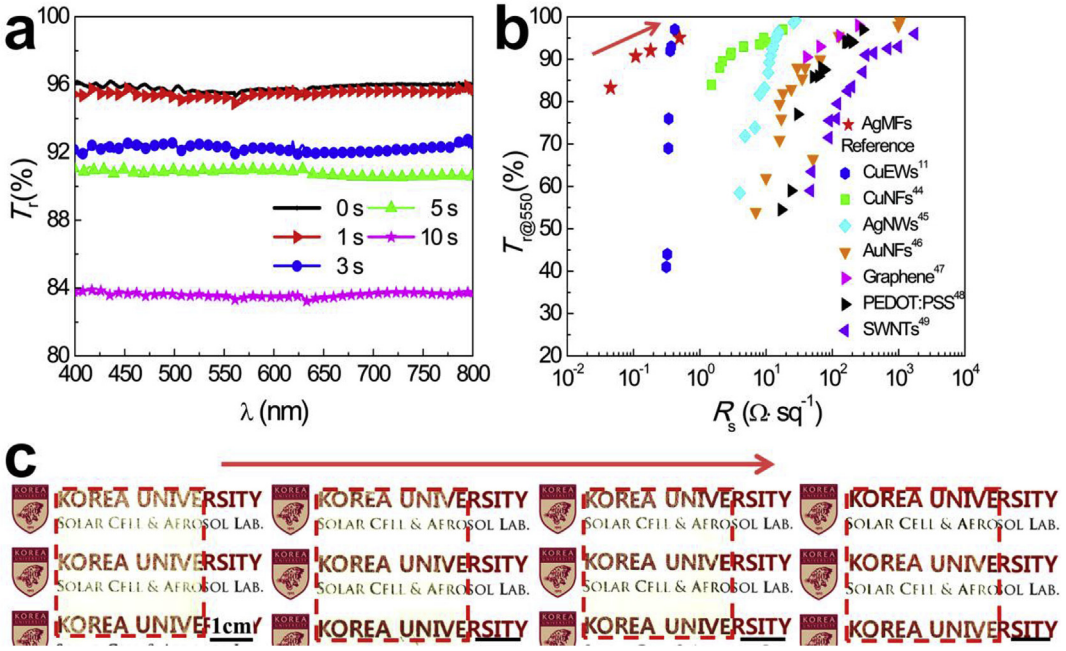

Fig. 4. (a) T_r spectra of the second AgMFs prepared using $V_{ep} = 5$ V with variation of t_{ep}. (b) T_r and R_s of the AgMFs as a function of t_{ep}: $t_{ep} = 10$, 5, 3, and 1 s from left to right, red stars. The T_r values of CuEWs, CuNFs, AgNWs, AuNFs, graphene, PEDOT:PSS, and SWNTs (single wall nanotube) are shown for comparison. (c) Photographs of the second AgMFs ($t_{ep} = 10$, 5, 3, and 1 s from left to right). (For interpretation of the references to color in this figure legend, the reader is referred to the Web version of this article.)

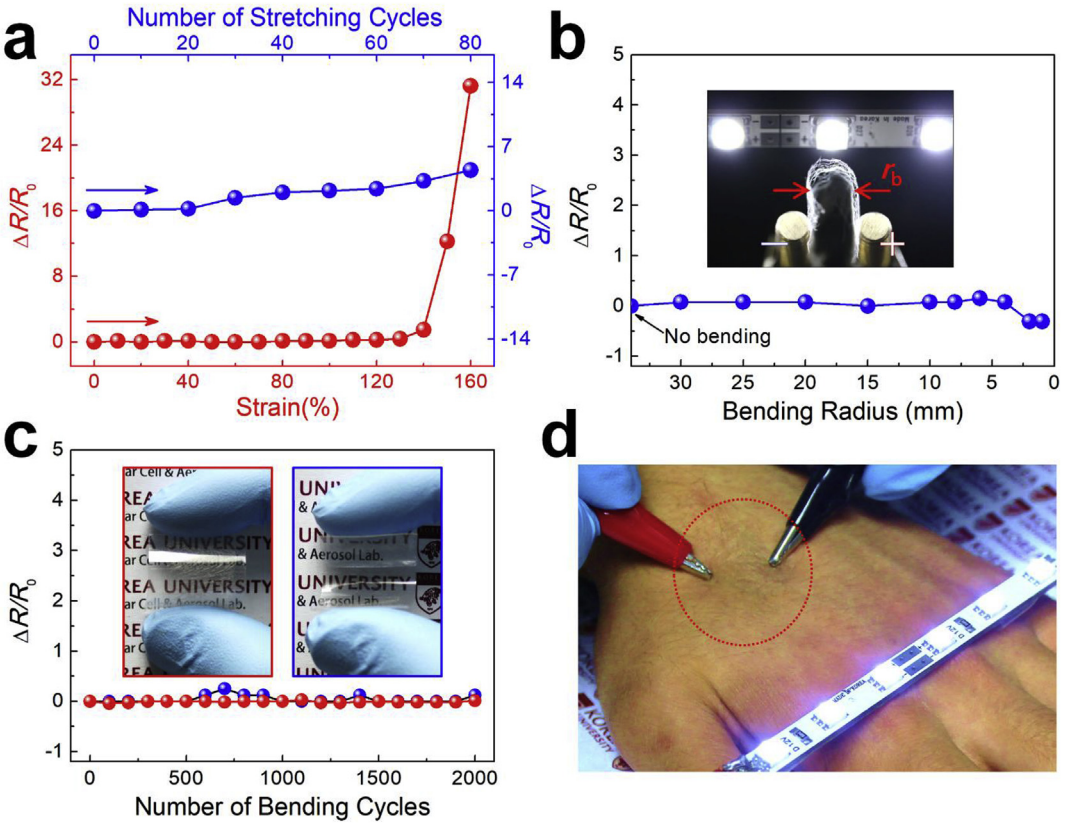

Fig. 5. (a) Results corresponding to uniaxial strain (red line) and stretching cycle tests (blue line). (b) Bending radius and (c) bending cycle tests [each color represents bending direction; the AgMFs were expanded (red line) and compressed (blue line)]. (d) A photograph of LED operation using the second AgMFs on a human hand ($t_{ep} = 3$ s, $V_{ep} = 5$ V). (For interpretation of the references to color in this figure legend, the reader is referred to the Web version of this article.)

(electrospinning time, cf. Sec. 2.), t_{ep}, V_{ep}, and I_{ep} (current density, cf. Sec. 2.), used for the different metal fibers arise from the corresponding differences in the extent of electroplating, metal type, *etc.* For the CuEWs, the average diameter, D_{avg}, values were not reported, although the R_s values were as low as 0.36–0.42 Ω sq^{-1} with $T_r = 92$–97%. The maximum T_r value of 97% for the CuEWs is 2% higher than that of the AgMFs ($T_r = 95$%). The comparison of the R_s values of the AgMFs and CuEWs at the same $T_r = 92$%, shows that

Table 3
T_r at the wavelength λ = 550 nm and the R_s values for comparison with previous studies by An et al. [11,12,38].

Case				Experimental result			*Ref*
Type	t_{es} (s)	t_{ep} (s)	V_{ep} or I_{ep}	D_{avg} (μm)	T_r (%)	R_s (Ω sq^{-1})	
AgMFs (2nd)	5	0	5 V	3.47 ± 0.17	96	3.01 ± 1.05	**Present study**
		1		5.17 ± 0.26	95	0.49 ± 0.01	
		3		6.50 ± 0.40	92	0.18 ± 0.03	
		5		8.35 ± 0.54	91	0.11 ± 0.04	
CuEWs	1	3	3 V	–	97	0.42	[11]
	5				93	0.37	
	6				92	0.36	
PtNFs	90	900	0.11 A cm^{-2}	0.64	55	14.1	[12]
		1800		0.82	48	4.32	
		2700		1.22	36	0.88	
NiEFs	5	60	0.22 A cm^{-2}	4.75	93	0.73	[38]
	30			3.85	83	0.49	
	60			3.77	64	0.30	

the R_s value for the AgMFs (R_s = 0.18 Ω sq^{-1}) is one-half of that of the CuEWs (R_s = 0.36 Ω sq^{-1}). For the PtNFs, the minimum t_{es} of 90 s is 90 times that of the AgMFs (t_{es} = 1 s), resulting in a T_r of 55%, lower than that of the AgMFs. In addition, the minimum t_{ep} is 900 s, 900 times longer than that of the AgMFs (t_{ep} = 1 s). Nevertheless, the D_{avg} value of the PtNFs is 0.64 μm, considerably lower than that of the AgMFs (D_{avg} = 3.47 μm), due to differences in the electroplating rates of Pt versus Ag. The R_s values of the PtNFs for transmittance values of T_r = 55% and 48% are 14.1 and 4.32 Ω sq^{-1}, respectively, which are larger than those of the other materials. Even though a rigorous comparison was not conducted in the present study, it seems that these results can be attributed to the different material properties and experimental conditions. The conditions used previously for the fabrication of NiEFs, t_{es} = 5 s and I_{ep} = 0.22 A cm^{-2} (Table 3), were used in the present study to fabricate the framework of the AgMFs (cf. Sec. 2.3.). Even though the same t_{es} and t_{ep} values were used, the obtained T_r and R_s values for the NiEFs in the previous and present studies (Table 3) are different because the other experimental conditions, such as the devices, temperature, and humidity, varied somewhat (not shown here).

Stretching and bending tests were performed to examine the stretchability and flexibility of the AgMFs prepared by the second electroplating method. Fig. 5a shows data for two different stretching tests. One applies uniaxial strain until the fiber mat breaks, whereas the other is a stretching cycle test over 80 cycles with repetitive stretching to 100% strain. In the uniaxial strain test, the resistance changes sharply above 140% strain and the fibers are broken at 160% strain (see Movie S1). In the stretching cycle test, a small change in the resistance is observed over 80 cycles. Fig. 5b shows the bending stability of the AgMFs for varying values of the bending radius r_b. The electrical properties of the mat are maintained until r_b is set to 1 mm from a flat mat. Note that light scattering from the background lighting makes the stand-alone fibers

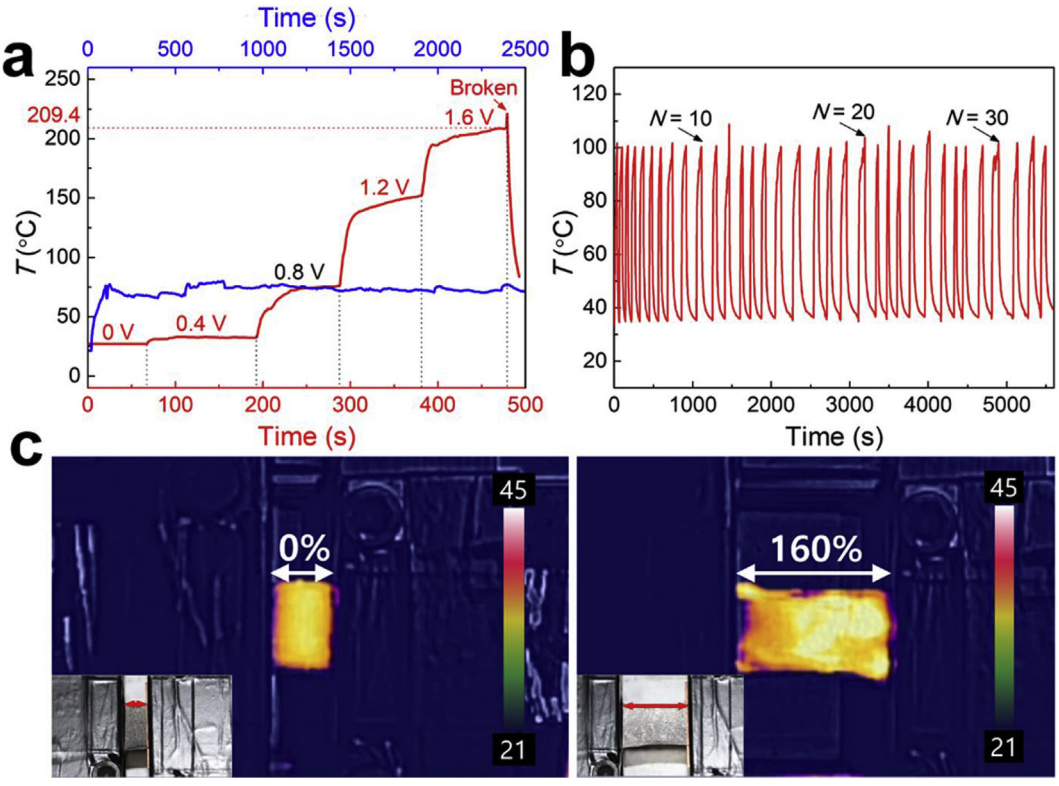

Fig. 6. Results of (a) heating tests and (b) heating cycle tests for the second AgMFs (t_{ep} = 3 s and V_{ep} = 5 V). (c) IR images during stretching.

distinctly visible in Fig. 5b. However, when the fibers are deposited on a transparent substrate as in Figs. 4c and 5c, they look quite transparent. A typical haze value of the metallized fiber electrode for a transparency of 91.3% is about 5%.

Fig. 5c shows the bending cycle data for the AgMFs. The electrical performance of the AgMFs remains constant for 2000 cycles even when the bending direction is changed (see the inset image of Fig. 5c), which induces expansion or compression of the sample [54]. The photograph in Fig. 5d shows LED operation using the highly transparent AgMFs, thus demonstrating the electrical stability of the AgMFs. The excellent mechanical and electrical stability of the AgMFs is expected to allow durability and facilitate application in various flexible electronic devices.

To characterize the heating performance of the second AgMFs as a transparent heater, both the heat generation and heat cycle performance were characterized as functions of the applied voltage and time, as depicted in Fig. 6. Fig. 6a shows the change in temperature (T) of the AgMFs at different applied voltages (V_a). The value of T increased from 27.3 to 209.4 °C as V_a increased from 0 to 1.6 V. Reversible heating of the AgMFs was observed in the 0–1.6 V range, although the AgMFs were degraded at voltage values $V_a > 2.0$ V. Furthermore, the performance of the AgMFs (*i.e.*, $T = 209.4$ °C at $V_a = 1.6$ V) is comparable to those of AgNWs ($T = 48–160$ °C) [48,55-58] and CNTs ($T = 77–160$ °C) [9,59-61] used as transparent heaters in previous studies, as well as those of graphene-based complexes ($T = 90–140$ °C) [62,63]. After a DC voltage $V_c = 0.8$ V is applied, T of the AgMFs rises sharply to 80 °C and is maintained continuously (the red line in Fig. 6a). There was no surface change observable by SEM imaging after heating (Fig. S7). The O content of the AgMFs before and after heating [measured by energy-dispersive X-ray spectroscopy (EDX)] was 4.40 wt% and 4.48 wt%, respectively. In the heat cycle test (Fig. 6b), the durability of the AgMFs was maintained even after 30 cycles. Fig. 6c shows the stretchability of AgMFs at a constant voltage. The heating performance is maintained until the AgMFs are stretched from 0% to 160% (see Movie S2). This flexible, stretchable, and transparent heater could be used as a smart window material for residences or automobiles that require high optical clarity [64]. In addition, the high thermal stability is expected to permit general applicability in wearable devices [65].

4. Conclusion

Core–shell-structured silver microfibers (AgMFs) with an intermediate Ni shell on PAN cores were fabricated using a combination of electrospinning and electroplating. The AgMFs produced using two different Ag-electroplating approaches were morphologically different, showing that the fabrication process can be tailored to produce specific morphologies to meet requirements for the intended end use of the MFs. The cactus-like morphology of the Ag fibers that maximizes the S/V ratio holds great promise for energy and environmental applications requiring maximal interfacial areas. In addition, subsequent deposition of other metallic layers was demonstrated, highlighting the potential for additional functions of such fibers. The AgMFs plated by the second method, with smoother surface morphology, exhibited remarkably high transmittance and low sheet resistance values, providing lower sheet resistance at transmittance up to 91% than any previously reported transparent electrodes. The AgMFs exhibited excellent mechanical performance and revealed no changes in electrical properties at 100% strain or after 80 repetitive stretching cycles or 2000 bending cycles. The AgMFs allowed resistive heating to 209 °C, which appears to be a record value compared to prior reports using Ag nanomaterials for transparent heaters. A heater temperature of 80 °C remained stable for over 500 s and 30 repetitive heating–cooling cycles. The thermal properties of the second type of AgMFs were thus significantly enhanced compared to those of previously reported materials. The second AgMFs have great potential for TCEs, smart windows, and wearable applications that require enhanced optical, mechanical, and thermal properties.

Acknowledgement

This research was supported by the Technology Development Program to Solve Climate Changes of the National Research Foundation (NRF) funded by the Ministry of Science, ICT & Future Planning (NRF-2016M1A2A2936760) and NRF-2017R1A2B4005639. This work was also supported by Advanced Research Center Program (NRF-2013R1A5A1073861) through the National Research Foundation of Korea (NRF) grant funded by the Korea government(MSIP).

Appendix A. Supplementary data

Supplementary data to this article can be found online at https://doi.org/10.1016/j.jallcom.2019.03.154.

References

[1] D.S. Leem, A. Edwards, M. Faist, J. Nelson, D.D. Bradley, J.C. de Mello, Efficient organic solar cells with solution-processed silver nanowire electrodes, Adv. Mater. 23 (2011) 4371–4375.
[2] Z. Yu, Q. Zhang, L. Li, Q. Chen, X. Niu, J. Liu, Q. Pei, Highly flexible silver nanowire electrodes for shape-memory polymer light-emitting diodes, Adv. Mater. 23 (2011) 664–668.
[3] J. Liang, L. Li, K. Tong, Z. Ren, W. Hu, X. Niu, Y. Chen, Q. Pei, Silver nanowire percolation network soldered with graphene oxide at room temperature and its application for fully stretchable polymer light-emitting diodes, ACS Nano 8 (2014) 1590–1600.
[4] M. Amjadi, A. Pichitpajongkit, S. Lee, S. Ryu, I. Park, Highly stretchable and sensitive strain sensor based on silver nanowire–elastomer nanocomposite, ACS Nano 8 (2014) 5154–5163.
[5] C.D. Bailie, M.G. Christoforo, J.P. Mailoa, A.R. Bowring, E.L. Unger, W.H. Nguyen, J. Burschka, N. Pellet, J.Z. Lee, M. Grätzel, Semi-transparent perovskite solar cells for tandems with silicon and CIGS, Energy Environ. Sci. 8 (2015) 956–963.
[6] Y. Joo, J. Byun, N. Seong, J. Ha, H. Kim, S. Kim, T. Kim, H. Im, D. Kim, Y. Hong, Silver nanowire-embedded PDMS with a multiscale structure for a highly sensitive and robust flexible pressure sensor, Nanoscale 7 (2015) 6208–6215.
[7] W.-J. Kwak, H.-G. Jung, S.-H. Lee, J.-B. Park, D. Aurbach, Y.-K. Sun, Silver nanowires as catalytic cathodes for stabilizing lithium-oxygen batteries, J. Power Sources 311 (2016) 49–56.
[8] S. Hu, T. Han, C. Lin, W. Xiang, Y. Zhao, P. Gao, F. Du, X. Li, Y. Sun, Enhanced electrocatalysis via 3D graphene aerogel engineered with a silver nanowire network for ultrahigh-rate zinc–air batteries, Adv. Funct. Mater. 27 (2017).
[9] L. Hu, H.S. Kim, J.-Y. Lee, P. Peumans, Y. Cui, Scalable coating and properties of transparent, flexible, silver nanowire electrodes, ACS Nano 4 (2010) 2955–2963.
[10] J.-G. Lee, J.-H. Lee, S. An, D.-Y. Kim, T.-G. Kim, S.S. Al-Deyab, A.L. Yarin, S.S. Yoon, Highly flexible, stretchable, wearable, patternable and transparent heaters on complex 3D surfaces formed from supersonically sprayed silver nanowires, J. Mater. Chem. A 5 (2017) 6677–6685.
[11] S. An, H.S. Jo, D.Y. Kim, H.J. Lee, B.K. Ju, S.S. Al-Deyab, J.H. Ahn, Y. Qin, M.T. Swihart, A.L. Yarin, Self-junctioned copper nanofiber transparent flexible conducting film via electrospinning and electroplating, Adv. Mater. 28 (2016) 7149–7154.
[12] S. An, Y.I. Kim, S. Sinha-Ray, M.-W. Kim, H.S. Jo, M.T. Swihart, A.L. Yarin, S.S. Yoon, Facile processes for producing robust, transparent, conductive platinum nanofiber mats, Nanoscale 9 (2017) 6076–6084.
[13] S. De, J.N. Coleman, The effects of percolation in nanostructured transparent conductors, MRS Bull. 36 (2011) 774–781.
[14] J. Xu, J. Hu, C. Peng, H. Liu, Y. Hu, A simple approach to the synthesis of silver nanowires by hydrothermal process in the presence of gemini surfactant, J. Colloid Interface Sci. 298 (2006) 689–693.
[15] B. Bari, J. Lee, T. Jang, P. Won, S.H. Ko, K. Alamgir, M. Arshad, L.J. Guo, Simple hydrothermal synthesis of very-long and thin silver nanowires and their application in high quality transparent electrodes, J. Mater. Chem. A 4 (2016) 11365–11371.
[16] Y.-J. Zhu, X.-L. Hu, Microwave-assisted polythiol reduction method: a new solid–liquid route to fast preparation of silver nanowires, Mater. Lett. 58 (2004) 1517–1519.
[17] Y. Yang, Y. Hu, X. Xiong, Y. Qin, Impact of microwave power on the

preparation of silver nanowires via a microwave-assisted method, RSC Adv. 3 (2013) 8431–8436.
[18] G. Riveros, S. Green, A. Cortes, H. Gomez, R. Marotti, E. Dalchiele, Silver nanowire arrays electrochemically grown into nanoporous anodic alumina templates, Nanotechnol 17 (2006) 561.
[19] Y. Zhou, S.H. Yu, C.Y. Wang, X.G. Li, Y.R. Zhu, Z.Y. Chen, A novel ultraviolet irradiation photoreduction technique for the preparation of single-crystal Ag nanorods and Ag dendrites, Adv. Mater. 11 (1999) 850–852.
[20] K. Zou, X.H. Zhang, X.F. Duan, X.M. Meng, S.K. Wu, Seed-mediated synthesis of silver nanostructures and polymer/silver nanocables by UV irradiation, J. Cryst. Growth 273 (2004) 285–291.
[21] Y. Sun, B. Mayers, T. Herricks, Y. Xia, Polyol synthesis of uniform silver nanowires: a plausible growth mechanism and the supporting evidence, Nano Lett. 3 (2003) 955–960.
[22] R.R. da Silva, M. Yang, S.-I. Choi, M. Chi, M. Luo, C. Zhang, Z.-Y. Li, P.H. Camargo, S.J.L. Ribeiro, Y. Xia, Facile synthesis of sub-20 nm silver nanowires through a bromide-Mediated polyol method, ACS Nano 10 (2016) 7892–7900.
[23] V. Thavasi, G. Singh, S. Ramakrishna, Electrospun nanofibers in energy and environmental applications, Energy Environ. Sci. 1 (2008) 205–221.
[24] Z. Dong, S.J. Kennedy, Y. Wu, Electrospinning materials for energy-related applications and devices, J. Power Sources 196 (2011) 4886–4904.
[25] K.A. Rieger, N.P. Birch, J.D. Schiffman, Designing electrospun nanofiber mats to promote wound healing–a review, J. Mater. Chem. B 1 (2013) 4531–4541.
[26] C. Zhou, Q. Shi, W. Guo, L. Terrell, A.T. Qureshi, D.J. Hayes, Q. Wu, Electrospun bio-nanocomposite scaffolds for bone tissue engineering by cellulose nanocrystals reinforcing maleic anhydride grafted PLA, ACS Appl. Mater. Interfaces 5 (2013) 3847–3854.
[27] A.L. Yarin, B. Pourdeyhimi, S. Ramakrishna, Fundamentals and Applications of Micro- and Nanofibers, Cambridge University Press, 2014.
[28] S. An, J.H. Hong, K.Y. Song, M.W. Lee, S.S. Al-Deyab, J.J. Kim, A.L. Yarin, S.S. Yoon, Prevention of mold invasion by eco-friendly lignin/polycaprolactone nanofiber membranes for amelioration of public hygiene, Cellulose 24 (2017) 951–965.
[29] S. Sinha-Ray, Y. Zhang, A. Yarin, Thorny devil nanotextured fibers: the way to cooling rates on the order of 1 kW/cm^2, Langmuir 27 (2010) 215–226.
[30] S. An, H.S. Jo, S.S. Al-Deyab, A.L. Yarin, S.S. Yoon, Nano-textured copper oxide nanofibers for efficient air cooling, J. Appl. Phys. 119 (2016), 065306.
[31] H. Yoon, M.-w. Kim, H. Kim, D.-Y. Kim, S. An, J.-G. Lee, B.N. Joshi, H.S. Jo, J. Choi, S.S. Al-Deyab, Efficient heat removal via thorny devil nanofiber, silver nanowire, and graphene nanotextured surfaces, Int. J. Heat Mass Transf. 101 (2016) 198–204.
[32] H.S. Jo, S. An, H.G. Park, M.-W. Kim, S.S. Al-Deyab, S.C. James, J. Choi, S.S. Yoon, Enhancement of critical heat flux and superheat through controlled wettability of cuprous-oxide fractal-like nanotextured surfaces in pool boiling, Int. J. Heat Mass Transf. 107 (2017) 105–111.
[33] H.S. Jo, S. An, J.-G. Lee, H.G. Park, S.S. Al-Deyab, A.L. Yarin, S.S. Yoon, Highly flexible, stretchable, patternable, transparent copper fiber heater on a complex 3D surface, NPG Asia Mater. 9 (2017).
[34] M.-w. Kim, H. Yoon, T.Y. Ohm, H.S. Jo, S. An, S.K. Choi, H. Park, S.S. Al-Deyab, B.K. Min, M.T. Swihart, Nanotextured cupric oxide nanofibers coated with atomic layer deposited ZnO-TiO 2 as highly efficient photocathodes, Appl. Catal., B 201 (2017) 479–485.
[35] D. Stauffer, A. Aharony, Introduction to Percolation Theory, CRC Press, Boca Raton, 1994.
[36] D. Stauffer, Scaling theory of percolation clusters, Phys. Rep. 54 (1979) 1–74.
[37] S. Duzyer, S. Sinha-Ray, S. Sinha-Ray, A.L. Yarin, Transparent conducting electrodes from conducting polymer nanofibers and their application as thin-film heaters, Macromol. Mater. Eng. (2017) 302.
[38] S. An, Y.I. Kim, H.S. Jo, M.-W. Kim, M.T. Swihart, A.L. Yarin, S.S. Yoon, Oxidation-resistant metallized nanofibers as transparent conducting films and heaters, Acta Mater. 143 (2018) 174–180.
[39] S. An, C. Lee, M. Liou, H.S. Jo, J.-J. Park, A.L. Yarin, S.S. Yoon, Supersonically blown ultrathin thorny devil nanofibers for efficient air cooling, ACS Appl. Mater. Interfaces 6 (2014) 13657–13666.
[40] X. Deng, C. Leys, D. Vujosevic, V. Vuksanovic, U. Cvelbar, N. De Geyter, R. Morent, A. Nikiforov, Engineering of composite organosilicon thin films with embedded silver nanoparticles via atmospheric pressure plasma process for antibacterial activity, Plasma Process. Polym. 11 (2014) 921–930.
[41] N.K. Vu, A. Zille, F.R. Oliveira, N. Carneiro, A.P. Souto, Effect of particle size on silver nanoparticle deposition onto dielectric barrier discharge (DBD) plasma functionalized polyamide fabric, Plasma Process. Polym. 10 (2013) 285–296.
[42] G.V. Rao, H. Shashikala, Optical, dielectric and mechanical properties of silver nanoparticle embedded calcium phosphate glass, J. Non-Cryst. Solids 402 (2014) 204–209.
[43] H. Wu, L. Hu, M.W. Rowell, D. Kong, J.J. Cha, J.R. McDonough, J. Zhu, Y. Yang, M.D. McGehee, Y. Cui, Electrospun metal nanofiber webs as high-performance transparent electrode, Nano Lett. 10 (2010) 4242–4248.
[44] H. Wu, D. Kong, Z. Ruan, P.-C. Hsu, S. Wang, Z. Yu, T.J. Carney, L. Hu, S. Fan, Y. Cui, A transparent electrode based on a metal nanotrough network, Nat. Nanotechnol. 8 (2013) 421–425.
[45] S. De, P.J. King, P.E. Lyons, U. Khan, J.N. Coleman, Size effects and the problem with percolation in nanostructured transparent conductors, ACS Nano 4 (2010) 7064–7072.
[46] S. Soltanian, R. Rahmanian, B. Gholamkhass, N.M. Kiasari, F. Ko, P. Servati, Highly stretchable, sparse, metallized nanofiber webs as thin, transferrable transparent conductors, Adv. Energy Mater. 3 (2013) 1332–1337.
[47] S. Bae, H. Kim, Y. Lee, X. Xu, J.-S. Park, Y. Zheng, J. Balakrishnan, T. Lei, H.R. Kim, Y.I. Song, Roll-to-roll production of 30-inch graphene films for transparent electrodes, Nat. Nanotechnol. 5 (2010) 574–578.
[48] T. Kim, Y.W. Kim, H.S. Lee, H. Kim, W.S. Yang, K.S. Suh, Uniformly interconnected silver-nanowire networks for transparent film heaters, Adv. Funct. Mater. 23 (2013) 1250–1255.
[49] V. Scardaci, R. Coull, J.N. Coleman, Very thin transparent, conductive carbon nanotube films on flexible substrates, Appl. Phys. Lett. 97 (2010), 023114.
[50] K.-S. Han, J.-H. Shin, H. Lee, Enhanced transmittance of glass plates for solar cells using nano-imprint lithography, Sol. Energy Mater. Sol. Cells 94 (2010) 583–587.
[51] A. Kim, Y. Won, K. Woo, C.-H. Kim, J. Moon, Highly transparent low resistance ZnO/Ag nanowire/ZnO composite electrode for thin film solar cells, ACS Nano 7 (2013) 1081–1091.
[52] W.J. Yu, S.H. Chae, S.Y. Lee, D.L. Duong, Y.H. Lee, Ultra-transparent, flexible single-walled carbon nanotube non-volatile memory device with an oxygen-decorated graphene electrode, Adv. Mater. 23 (2011) 1889–1893.
[53] P. Kuang, J.M. Park, W. Leung, R.C. Mahadevapuram, K.S. Nalwa, T.G. Kim, S. Chaudhary, K.M. Ho, K. Constant, A new architecture for transparent electrodes: relieving the trade-off between electrical conductivity and optical transmittance, Adv. Mater. 23 (2011) 2469–2473.
[54] Z. Hao, L. Yuan-Yuan, Y. Mei-Yin, Z. Bao, Y. Guang, W. Shou-Guo, W. Kai-You, Tuning the magnetic anisotropy of CoFeB grown on flexible substrates, Chin. Phys. B 24 (2015), 077501.
[55] R. Gupta, K. Rao, K. Srivastava, A. Kumar, S. Kiruthika, G.U. Kulkarni, Spray coating of crack templates for the fabrication of transparent conductors and heaters on flat and curved surfaces, ACS Appl. Mater. Interfaces 6 (2014) 13688–13696.
[56] P.-C. Hsu, X. Liu, C. Liu, X. Xie, H.R. Lee, A.J. Welch, T. Zhao, Y. Cui, Personal thermal management by metallic nanowire-coated textile, Nano Lett. 15 (2014) 365–371.
[57] S. Sorel, D. Bellet, J.N. Coleman, Relationship between material properties and transparent heater performance for both bulk-like and percolative nanostructured networks, ACS Nano 8 (2014) 4805–4814.
[58] S. Hong, H. Lee, J. Lee, J. Kwon, S. Han, Y.D. Suh, H. Cho, J. Shin, J. Yeo, S.H. Ko, Highly stretchable and transparent metal nanowire heater for wearable electronics applications, Adv. Mater. 27 (2015) 4744–4751.
[59] Y.H. Yoon, J.W. Song, D. Kim, J. Kim, J.K. Park, S.K. Oh, C.S. Han, Transparent film heater using single-walled carbon nanotubes, Adv. Mater. 19 (2007) 4284–4287.
[60] H.-S. Jang, S.K. Jeon, S.H. Nahm, The manufacture of a transparent film heater by spinning multi-walled carbon nanotubes, Carbon 49 (2011) 111–116.
[61] D. Jung, D. Kim, K.H. Lee, L.J. Overzet, G.S. Lee, Transparent film heaters using multi-walled carbon nanotube sheets, Sensor Actuator Phys. 199 (2013) 176–180.
[62] J. Kang, H. Kim, K.S. Kim, S.-K. Lee, S. Bae, J.-H. Ahn, Y.-J. Kim, J.-B. Choi, B.H. Hong, High-performance graphene-based transparent flexible heaters, Nano Lett. 11 (2011) 5154–5158.
[63] J. Kang, Y. Jang, Y. Kim, S.-H. Cho, J. Suhr, B.H. Hong, J.-B. Choi, D. Byun, An Ag-grid/graphene hybrid structure for large-scale, transparent, flexible heaters, Nanoscale 7 (2015) 6567–6573.
[64] M. Kamalisarvestani, R. Saidur, S. Mekhilef, F. Javadi, Performance, materials and coating technologies of thermochromic thin films on smart windows, Renew. Sustain. Energy Rev. 26 (2013) 353–364.
[65] F. Wang, C. Gao, K. Kuklane, I. Holmér, A review of technology of personal heating garments, Int. J. Occup. Saf. Ergon. 16 (2010) 387–404.